

## Annealing kinetics of {311} defects and dislocation loops in the end-of-range damage region of ion implanted silicon

L. S. Robertson<sup>a)</sup> and K. S. Jones

*Department of Materials Science and Engineering, University of Florida, Gainesville, Florida 32611*

L. M. Rubin and J. Jackson

*Eaton Corporation, Beverly, Massachusetts 01915*

(Received 3 November 1999; accepted for publication 15 December 1999)

The evolution of both {311} defects and dislocation loops in the end-of-range (EOR) damage region in silicon amorphized by ion implantation was studied by *ex situ* transmission electron microscopy (TEM). The amorphization of a (100) *n*-type Czochralski wafer was achieved with a 20 keV  $1 \times 10^{15}/\text{cm}^2$   $\text{Si}^+$  ion implantation. The post-implantation anneals were performed in a furnace at 750 °C for times ranging from 10 to 370 min. After annealing the specimen for 10 min, the microstructure showed a collection of both {311} defects and small dislocation loops. The evolution of a specific group of defects was studied by repeated imaging of the same region after additional annealing. Quantitative TEM showed that {311} defects followed one of two possible evolutionary pathways as annealing times progressed; unfaulting to form dislocation loops or dissolving and releasing interstitials. Results indicate that in this temperature regime, {311} defects are the preferential site for dislocation loop nucleation. © 2000 American Institute of Physics.

[S0003-6951(00)00807-X]

Ion implantation is an integral step in current integrated circuit (IC) processing. Energetic ions which impinge upon the silicon wafer during implantation cause significant damage to the silicon lattice. At sufficient energies and doses of ions, the implantation produces an amorphous layer on the surface of the wafer. During post-implantation annealing, the amorphous layer recrystallizes via solid phase epitaxial regrowth at approximately 600 °C. Following regrowth, a damaged layer termed the end-of-range (EOR) damage region remains below the former amorphous-to-crystalline (*a/c*) interface. The EOR contains a supersaturation of excess interstitial point defects resulting from transmitted ions and recoiled atoms during the implantation. At higher temperatures, the excess interstitials in the EOR both diffuse away to regions of lower interstitial concentration and precipitate into EOR (type II) extended defects.<sup>1</sup> These extended defects can lead to the two main difficulties in creating shallow junctions in amorphized layers: leakage current from defects in the space charge region of the device<sup>2</sup> and junction depth increase by transient enhanced diffusion of the dopant. For these reasons, understanding the evolution kinetics of extended defects in the EOR is an essential step in creating accurate process models for future generations of ICs.

One aspect of the evolution kinetics of EOR extended defects that has been speculated about for many years, and to date remains in question, is the nature of dislocation loop nucleation in the EOR. Some authors have proposed models for the homogeneous dislocation loop nucleation.<sup>3</sup> Others argue the existence of different heterogeneous nucleation sites. Wu *et al.*<sup>4</sup> suggested that EOR dislocation loops nucleate by the collapse of isolated amorphous pockets below the *a/c*

interface during annealing. Hiraga and Hirabayashi proposed impurities such as oxygen or carbon may serve as nucleation sites.<sup>5</sup> Recently, Li and Jones showed that, for nonamorphizing implantations, {311} defects serve as the nucleation site for subthreshold dislocation loops<sup>6</sup> in silicon and are in fact “the source of the loops.” Since many differences exist between the behavior of impurities and point defects in amorphized versus nonamorphized silicon, in this letter, we seek to determine if the same behavior holds for amorphized silicon.

A (100) *n*-type Czochralski silicon wafer was implanted using an Eaton NV-GSD 200E. The wafer was amorphized using a  $\text{Si}^+$  implantation, with an energy of 20 keV at a dose of  $1 \times 10^{15}/\text{cm}^2$ , which created a continuous amorphous layer. The dose rate of the implant was maintained at 0.3 mA/cm<sup>2</sup>, while the endstation temperature was maintained at  $20 \pm 1$  °C. The ion beam was tilted 5° off the wafer normal towards the (110) direction. Post-implantation annealing was performed in a tube furnace at 750 °C in a  $\text{N}_2$  ambient. Annealing times ranged from 15 to 370 min. After an initial anneal of 15 min at 750 °C, the sample was made into a plan-view transmission electron microscopy (TEM) specimen by first mechanically polishing the sample to a thickness  $\approx 100$  μm and then chemically etching the sample from the backside using a HF:HNO<sub>3</sub> (ratio of 1:3) solution to create a specimen with a thin region suitable for viewing in a TEM. A JEOL 200CX TEM was then used to take micrograph images of the specimen. The micrographs were taken under weak beam dark field imaging conditions with a  $g=[220]$  two-beam diffraction condition. The imaging of particular regions in the specimen as a function of *ex situ* annealing time was performed at 750 °C. More specifically, a region of a specimen was imaged, the sample was removed from the

<sup>a)</sup>Electronic mail: lancer@grove.ufl.edu

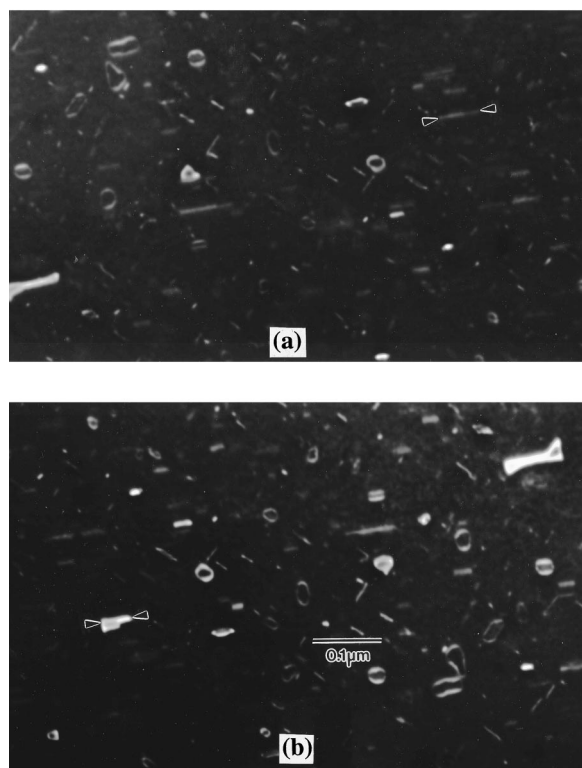


FIG. 1. Plan-view TEM images of the extended defects in the EOR showing  $\{311\}$  defects transforming into dislocation loops. Samples annealed at 750 °C for (a) 57 min and (b) 75 min. The  $\{311\}$  defect indicated by the arrows in (a) corresponds to the loop indicated by the arrows in (b).

TEM, annealed in a tube furnace (*ex situ*) and imaged in the TEM once more after the annealing interval. Care was taken in specimen handling in order to maintain specimen integrity. The specimen was carefully positioned in the specimen cup of the TEM to insure uniform orientation of the specimen with respect to the electron beam. The exact diffracting conditions, nominally  $g=[220]$ , were maintained throughout the experiment for identical imaging conditions. The two main types of defects observed in the TEM were  $\{311\}$  defects and dislocation loops. The concentration of interstitials bound by the  $\{311\}$  defects was found using an image processor to find the projected line length of the defects from a micrograph. An assumption of constant defect width of 60 Å was used to find the interstitial concentration by multiplying the line length by 26 interstitials/nm and then dividing by the area observed to yield the number of interstitials per  $\text{cm}^2$ . A similar process was used in the analysis of the dislocation loops, however, in this case, a stereographic grid technique was used to find the area of the loops. The areal fraction of the loops was multiplied by  $1.6 \times 10^{15}/\text{cm}^2$ , the approximate atomic density on the  $\{111\}$  plane.

The evolution of extended defects in the EOR is shown in the series of micrographs in Fig. 1. The images show that the number of  $\{311\}$  defects is decreasing with increasing annealing time and the number of loops is increasing with increasing annealing time. The defect labeled ‘a’ is seen to evolve from a  $\{311\}$  defect in Fig. 1(a) to a dislocation loop in Fig. 1(b). Both the number of extended defects and the number of interstitials bound by the extended defects were

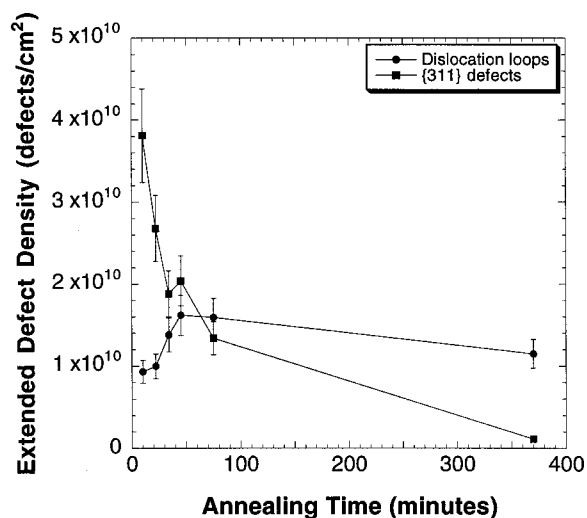


FIG. 2. Density of extended defects in the EOR as function of annealing time at 750 °C.

quantified in Figs. 2 and 3, respectively. As evident from Figs. 2 and 3, both the number of dislocation loops and the interstitials bound by dislocation loops increases with increasing annealing time, whereas the number of  $\{311\}$  defects and interstitials bound by  $\{311\}$  defects decreases with increasing time. The number of  $\{311\}$  defects which disappear,  $3.7 \pm 0.5 \times 10^{10}/\text{cm}^2$ , was over ten times greater than the number of dislocation loops observed to nucleate,  $2.2 \pm 0.2 \times 10^9/\text{cm}^2$ , indicating that  $\{311\}$  unfaulding is a viable mechanism for the nucleation of the dislocation loops in this time interval in terms of conservation of defects sites. The number of interstitials released by  $\{311\}$  defects over this time interval was  $3.0 \pm 0.5 \times 10^{13}/\text{cm}^2$  and the number of interstitials captured by dislocation loops was  $4.6 \pm 0.5 \times 10^{13}/\text{cm}^2$ . A plot of the percentage of dislocation loops formed as a function of annealing time is shown in Fig. 4. The percentage of the loops formed was calculated using the sum of the number of loops observed to form and the initial number of loops as the total. A small number ( $\sim 15\%$ ) of the

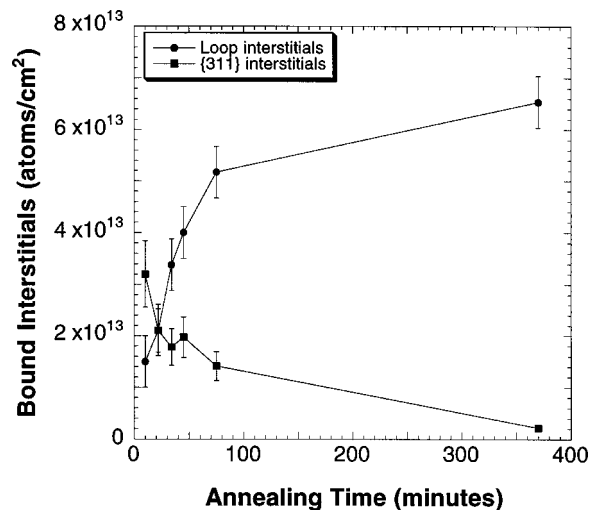


FIG. 3. Density of interstitials bound by extended defects in the EOR as function of annealing time at 750 °C.

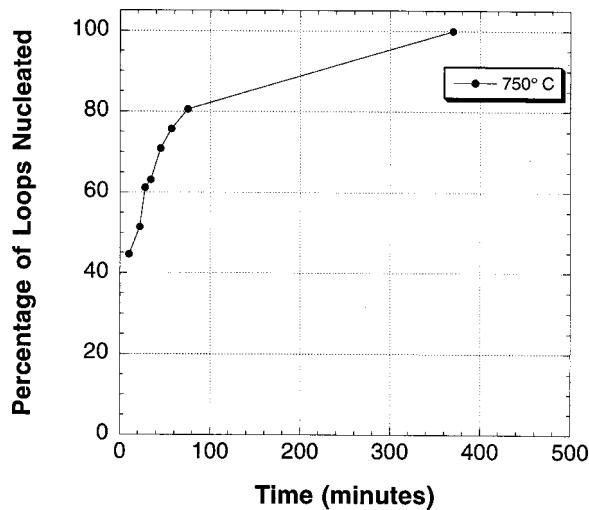


FIG. 4. Percent of final number of EOR dislocation loops nucleated as a function of annealing time at 750 °C.

dislocation loops dissolved in the interval between 75 and 370 min. For the plot in Fig. 4, the dissolution was ignored and only the addition of loops observed to nucleate was considered. From Fig. 4 it is apparent that 45% of the loops had nucleated by 10 min at 750 °C. The nucleation site of each dislocation loop observed to nucleate was studied by comparing sequential micrograph images. The loops that nucleated did so either from a {311} defect site or at a site where no perturbation of the lattice visible by TEM was observable. The percentage of the loops that nucleated at {311} defect sites is plotted in Fig. 5. The average percentage loops that nucleated at {311} defect sites during the interval from 10 to 370 min was approximately 75%. Recognizing that the sample under observation had been thinned prior to annealing and experienced several temperature ramps, the effect of sample thickness and temperature ramping were investigated by comparing four samples, A, B, C, and D, each annealed at 750 °C for 75 min. Samples A and B were annealed prior to

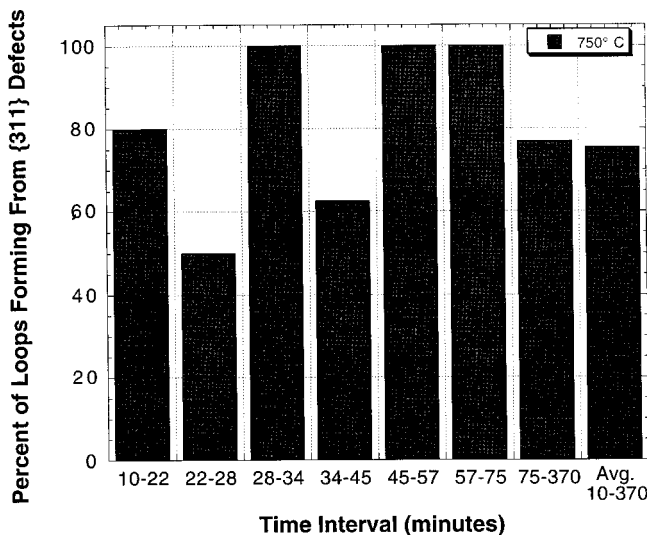


FIG. 5. Percent of EOR dislocation loops nucleating at {311} defect sites at each time interval observed at 750 °C.

thinning, samples C and D were annealed after thinning. Samples B and C were annealed in 11 time intervals, samples A and D were annealed in 2 time intervals. Neither factor had an observable effect on the final density or size distribution of the EOR defects in the samples.

Of the aforementioned data the most salient point is that the majority of the dislocation loops observed to nucleate did so at {311} defects indicating that at 750 °C, {311} unfauling is the preferential path of dislocation loop nucleation. Understanding the mechanism of loop nucleation is an important step in the process of determining the evolution kinetics of point and extended defects in ion implanted silicon. As set forth in a previous paper by Li and Jones,<sup>6</sup> the possible unfauling reactions of a {311} to a dislocation loop are as follows:

$$\text{Frank loops} \Rightarrow a/2[116] + a/2[661] = a/3[111],$$

$$\text{Shockley loops} \Rightarrow a/2[116] + a/42[19\bar{2}9] = a/2[101].$$

Systematic study of the habit plane of EOR dislocation loops has previously shown that loops reside on the {111} planes,<sup>7</sup> whereas {311} defects reside on the {311} plane.<sup>8,9</sup> Therefore, nucleation of a dislocation loop by the unfauling of a {311} defect also involves the climb of the interstitials from the {311} plane to the final habit plane either during or immediately after the unfauling reaction.

The direct observation of the unfauling reaction of the {311} defect transforming into a dislocation loop is a powerful result of this work. The other data support the assertion that this is not merely a statistical anomaly. Other authors have observed that in the EOR, at short times at moderate temperatures, there is initially a large number of {311} defects and a smaller number of dislocation loops.<sup>10-12</sup> With the progression of annealing to longer times, the number of {311} defects decreases and the number of dislocation loops increases. At longer times and higher temperatures, {311} defects disappear and only dislocation loops remain. These data indicate that {311} defects serve as intermediate defects in the silicon lattice.

One question raised by the results of this experiment is the nature of the origin of the ~25% of the loops which do not appear to nucleate from {311} defects. In a previously published paper,<sup>6</sup> the authors report that all of the dislocation loops observed to nucleate did so at {311} defect sites. The authors of this letter assert that {311} defect sites serve as the preferential site for dislocation loop nucleation, and several possible explanations are able to account for the origin of the remaining 25% of the loops.

Images of extended defects in silicon are obtained because of the lattice strain around the defects. All extended defects have a certain amount of strain associated with them, however not all defects are visible under a single imaging conditions. Theoretically, roughly 85% of all possible {311} defect configurations are visible under a single  $\mathbf{g}=[220]$  imaging condition, using the  $\mathbf{g}\cdot\mathbf{b}=0$  invisibility criterion (assuming those defects do not have  $\mathbf{g}\cdot\mathbf{b}\times\mathbf{u}>0.64$ ). However, the ability to image defects in a TEM is dependent both upon the contrast and brightness of the defect image. Both brightness and contrast are functions of the deviation parameter

$s_g$ . Small variations in  $s_g$  have dramatic effects on contrast and brightness. These variations can determine whether a defect will have residual contrast in spite of fulfilling the invisibility criterion. Additionally, the brightness of an image is a function of the strain field of the defect. The strain field of a defect is directly proportional to its Burger's vector. Since the numerical value of the Burger's vector in angstroms is 0.294 for a {311} defect and 0.577 for a Frank loop and 0.707 for a Shockley loop, the brightness of the loops is much greater than that of the {311} defects. Given these conditions, it is conceivable that a {311} could exist yet be invisible via TEM, then after unfaulting become visible.

Another possibility that accounts for the 25% of the loops not observed to nucleate from {311} defects is that those loops nucleated at a submicroscopic interstitial cluster (SMIC). The existence of SMICs in this sample is suggested by the inability of the release of interstitials from {311} defects to account for the growth in the number of interstitials bound by the dislocation loops. The structure of SMICs is not known. It is possible that a SMIC may merely be a small {311} defect, since the minimum size for a {311} defect that may be imaged in conventional TEM is approximately 100 atoms. It may also be an interstitial cluster with a stable number of interstitials below the resolution of TEM, i.e.,  $n = 8$ .<sup>13</sup> In the work by Li and Jones, the nucleation stage had progressed farther initially compared to the present work as evidenced by the fact that the first data point in Li and Jones corresponded to 60% of the dislocation loops already nucleated versus 45% for the present work. If SMICs are small {311} defects, then it would seem plausible that some of the nucleation sites would be smaller defect sites compared to earlier work by Li and Jones.<sup>6</sup>

In conclusion, the kinetics of extended defect evolution

in the EOR, both {311} defects and dislocation loops, have been investigated quantitatively via *ex situ* TEM. It has been shown that {311} defects serve as the preferential site for dislocation loop nucleation, which correlates to previous findings for nonamorphizing implants. These conclusions provide not only a source of EOR dislocation loops but also yield the two possible evolutionary pathways for {311} defects; dissolution and unfaulting. Since {311} defects are presumed to be the source of interstitials for TED, the results of this work imply that process models must account for both the dissolution and unfaulting of {311} defects in order to accurately predict diffusion of dopant atoms in regions where an amorphizing implantation has been performed.

<sup>1</sup>K. S. Jones, S. Prussin, and E. R. Weber, *Appl. Phys. A: Solids Surf.* **45**, 1 (1988).

<sup>2</sup>E. Landi and S. Solmi, *Solid-State Electron.* **29**, 1181 (1986).

<sup>3</sup>T. Y. Tan, *Philos. Mag. A* **44**, 101 (1981).

<sup>4</sup>N. R. Wu, P. Ling, D. K. Sadana, J. Washburn, and M. I. Current, *Proceedings of Electrochemical Society (ECS, New York, 1983)*, p. 366.

<sup>5</sup>K. Hiraga and M. Hirabayashi, *Proceedings of the Seventh International Conference on High Voltage Electron Microscopy, Berkeley, 1983*, p. 175.

<sup>6</sup>J.-H. Li and K. S. Jones, *Appl. Phys. Lett.* **73**, 3748 (1998).

<sup>7</sup>B. de Mauduit, L. Laanab, C. Bergaud, M. M. Faye, A. Martinez, and A. Claverie, *Nucl. Instrum. Methods Phys. Res. B* **84**, 190 (1994).

<sup>8</sup>S. M. Davidson and G. R. Booker, *Radiat. Eff.* **6**, 33 (1970).

<sup>9</sup>S. Takeda, M. Kohyama, and K. Ibe, *Philos. Mag. A* **70**, 287 (1994).

<sup>10</sup>K. S. Jones, L. H. Zhang, V. Krishnamoorthy, M. Law, D. S. Simons, P. H. Chi, L. Rubin, and R. G. Elliman, *Appl. Phys. Lett.* **68**, 2672 (1996).

<sup>11</sup>K. S. Jones, M. K. J. Chen, M. Puga-Lambers, B. Freer, J. Berstein, and L. Rubin, *J. Appl. Phys.* **81**, 6051 (1997).

<sup>12</sup>G. Z. Pan, K. N. Tu, and S. Prussin, *Appl. Phys. Lett.* **71**, 659 (1997).

<sup>13</sup>N. E. B. Cowern, G. Mannino, P. A. Stolk, F. Roozeboom, H. G. A. Huizing, J. G. M. van Berkum, F. Cristiano, A. Claverie, and M. Jaraiz, *Phys. Rev. Lett.* **82**, 4460 (1999).